

Ocean surface determination from X-band radar-image sequences

H. Dankert and W. Rosenthal

GKSS Research Center, Geesthacht, Germany

Received 19 September 2003; revised 13 January 2004; accepted 2 March 2004; published 20 April 2004.

[1] An empirical inversion method is presented for determination of time series of ocean surface elevation maps from nautical radar-image sequences. The method is based on the determination of the surface tilt angle in antenna look direction at each pixel of the radar images. Thereby in situ sensors are not required. An external calibration is not necessary. A conventional nautical X-band radar, operating at grazing incidence and horizontal polarization in transmit and receive, is used as a sensor. Radar-image sequences, with their high spatial resolution and large coverage, offer a unique opportunity to derive and study individual waves and wave fields in space and time and therefore allow the measurement of individual wave parameters and wave groups. For validation of the inversion scheme, the significant wave heights derived from the inverted radar data sets and from colocated wave records are compared. It is shown that the accuracy of the radar-retrieved significant wave height is within the accuracy of the in situ sensors. Furthermore, a wave elevation time series is directly compared to a buoy record to show the capabilities of the proposed method. *INDEX TERMS*: 4275 Oceanography: General: Remote sensing and electromagnetic processes (0689); 3360 Meteorology and Atmospheric Dynamics: Remote sensing; 3384 Meteorology and Atmospheric Dynamics: Waves and tides; 4560 Oceanography: Physical: Surface waves and tides (1255); *KEYWORDS*: inversion, ocean surface, marine radar

Citation: Dankert, H., and W. Rosenthal (2004), Ocean surface determination from X-band radar-image sequences, *J. Geophys. Res.*, 109, C04016, doi:10.1029/2003JC002130.

1. Introduction

[2] The ocean surface elevation is typically measured with one-dimensional (1-D) in situ sensors such as buoys, laser sensors, or wave gauges with high accuracy. These sensors are placed on certain and carefully chosen positions in measurement areas, offshore close to platforms, near-shore areas, or in harbors. Offshore, the sea state conditions are typically homogeneous; the statistical properties of the sea surface are not changing from one location to the next in the measurement area. Close to the coast, inside harbors or behind offshore and nearshore buildings and structures, the sea state becomes inhomogeneous. The sea state parameters, which have been measured by the 1-D in situ sensors, are not transmissible to neighboring locations. Further, there is a lack of directional information about the wave fields. The sea state is therefore incompletely captured by such sensors. The possible positions of such sensors is limited on the mooring requirements, for example, for a wave rider buoy the given water depth and the maximum current speed are important. The shortcomings of point sensors are overcome by spatially and temporally measuring sensors like mapping radar instruments.

[3] In this paper a radar-based remote sensing technique is introduced to measure the ocean surface elevation, both spatially and temporally. A nautical radar operating at

X-band with HH polarization is used that has the capability of measuring the backscatter from the ocean surface in space $\vec{r} = (x, y)$ and time t under most weather conditions, independent of light conditions [Young *et al.*, 1985]. The radar scans temporal sequences of consecutive radar images of the ocean surface $\eta(\vec{r}, t)$ at grazing incidence from towers and ships. The investigations presented in this study were performed with data sets collected by a radar system installed aboard a platform in the Norwegian oil field Ekofisk in the central North sea using the Wave Monitoring System (WaMoS). This system uses a conventional nautical radar as sensor.

[4] In addition to the ocean surface retrieval presented here, nautical radar image sequences of the sea surface are also used to determine other hydrographic parameters. In particular, they have been used to determine two-dimensional wave-spectra and significant wave heights [Borge *et al.*, 1999], individual wave parameters [Borge *et al.*, 2004], wave groups [Dankert *et al.*, 2003a], the near-surface current [Senet *et al.*, 2001], and bathymetry [Bell, 1999; Trizna, 2001]. Recently, new methods for the current and bathymetry field retrieval from nautical radar image sequences have been developed [Dankert, 2003]. Nautical radar image sequences are further used for the retrieval of high-resolution ocean wind fields [Dankert *et al.*, 2003b].

[5] Ocean waves are imaged by a nautical radar because the long surface gravity waves modulate the radar back-

scatter from the sea surface. Thereby the small-scale roughness of the sea surface, which is generated by the local wind field, raises the backscatter of the ocean surface [Lee *et al.*, 1995; Trizna, 1997]. At moderate incidence angles the modulation is mainly due to the tilt and hydrodynamic modulation [Alpers *et al.*, 1981], while at grazing incidence the modulation stems also from the shadowing of the radar beam due to the ocean waves [Wetzel, 1990]. These modulation mechanisms contribute to the imaging of surface waves whose wavelengths are greater than 2 times the radar resolution.

[6] The square root of the signal-to-noise ratio (SNR) of nautical radar-image sequences is proportional to the significant wave height of the observed wave field [Ziemer, 1995]. This is in accordance with the synthetic aperture radar (SAR), where the SNR is also used for the calibration of the image spectra [Alpers and Hasselmann, 1982; Plant, 1991]. The calibration of image spectra using the SNR is based on the assumption that the radar backscatter in the analyzed area is a Gaussian distribution [Alpers and Hasselmann, 1982]. During the calibration phase for the radar-image sequence image spectra the calibration constants have to be determined by taking colocated in situ measurements, for example, from buoy or laser measurements. After this calibration phase the system works as a stand-alone instrument. On the basis of this technique, Borge *et al.* [2004] have introduced an inverse modeling technique for retrieving the ocean surface elevation. The method is based on the determination of the modulation transfer function (MTF) between the radar image spectrum and an in situ sensor heave spectrum. To obtain the MTF, a calibration phase needs to be carried out. The estimated MTF is applied to the amplitudes of the complex radar image spectrum and only to those components that contain spectral energy of the linear surface gravity waves. The phases of these components are also retained.

[7] This paper introduces an empirical method for the determination of the ocean surface elevation in space and time for the radar-image sequences. Thereby no in situ measurements are required. An external calibration is not necessary. Hydrodynamic modulation is neglected here. The geometrical effect of shadowing is assumed to have a minor contribution to the RCS. The method is based on the determination of the surface tilt angle in antenna look direction at each pixel of the radar images. The mean radar cross section (RCS) depends on the mean local depression angle. This dependency is parameterized as a look-up table. The idea is that the deviation of the RCS from the mean RCS represents a local and temporal change of the depression angle, which is assumed to be equal to the local ocean surface tilt. The translation of the RCS to the local surface tilt is a local, spatial, and temporal description of the modulation process. Up to now, the modulation processes were described in the Fourier domain.

[8] The method is very robust and should work especially well if the main modulation of the RCS comes from the local surface slope in antenna look direction (tilt modulation). It will perform well even if the relation between tilt and RCS is nonlinear.

[9] For validation of the method, colocated measurements from three in situ sensors, one wave rider buoy and two laser sensors, were taken. The validation phase is divided

into two steps. In the first step, a comparison of the significant wave height as statistical integral spectral parameter from the inverted radar-image sequences and the colocated in situ data is performed. The second phase is a deterministic comparison. Subsequently, a wave profile measured by the buoy is compared to the colocated radar-derived ocean surface time series at the location of the buoy. The wave rider buoy is thereby directly seen by the radar. The laser sensors are also located in the measurement area of the radar, but in a shadowed region, and therefore are unsuitable for this direct comparison.

[10] The paper is organized as follows: In section 2 the radar system and available data are introduced. Section 3 gives a theoretical introduction into the radar imaging processes. In section 4 the ocean surface retrieval algorithm is introduced and applied to radar data sets. The radar retrieved significant wave heights are compared to the colocated in situ values in section 5. Further, a deterministic comparison is performed and the retrieved spectra are considered. Finally, in section 6, conclusions and an outlook are given.

2. Investigated Data

[11] The measurements have been carried out from the platform “2/4k” of the Ekofisk oil field operated by ConocoPhillips in the North Sea at 56.5°N and 3.2°E. The water depth in this area is about 70 m. The radar measurements are performed operationally by a typical nautical radar together with a WaMoS II unit, which allows for the continuous digitization of time series of polar nautical radar images. They are used for the determination of 2-D wave spectra and integral sea state parameters like peak wavelength, peak period, and the estimation of the significant wave height in comparison to a common wave rider buoy and two laser sensors in this area. The near-surface current velocity is estimated. The radar data are compared to colocated synthetic aperture radar (SAR) measurements. Furthermore, the radar-image sequences are used for the determination of high-resolution wind vector fields [Dankert *et al.*, 2003b].

[12] In Figure 1 the platform, the location of the installed radar system, the in situ sensors, and a recorded sample radar-image sequence are shown. The nautical radar was operated at 9.5 GHz (X-band) with horizontal (HH) polarization in transmit and receive at grazing incidence. The radar antenna is installed at the northwest corner of the platform marked by the black arrow. The installation height of the antenna is 74 m above the mean sea level. The radar system is operationally recording data sets of 32 images. The time interval between two consecutive images is $\Delta t = 2.56$ s. A complete time series therefore covers a time period of $T_{tot} \approx 82$ s. The radar covers an area within a radius of about 2 km. The polar images are converted to rectangular coordinates. The grid size is chosen to be equal to the radar resolution of $\Delta r \approx 10$ m. The radar-image sequence shows a wave field, which is propagating in a northerly direction. The dark patches in the radar images are due to the platform equipment, for example, the helicopter deck and the lattice towers. The higher backscatter in the south originates from the other platforms of the oilfield, which are also visible in the foreground of the photo. For

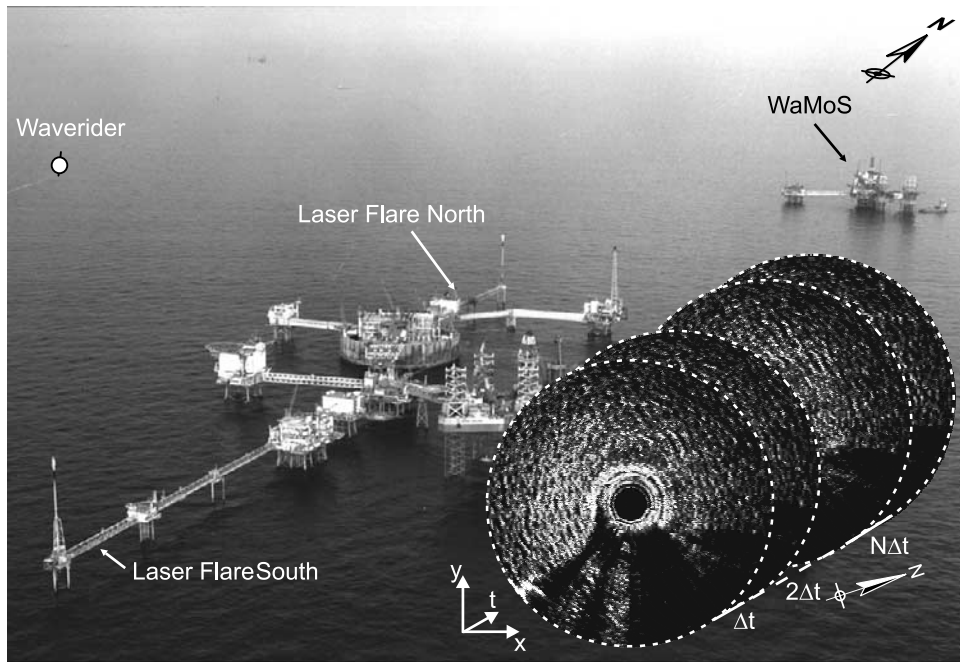


Figure 1. Ekofisk 2/4k platform of the Ekofisk oil field in the North Sea. The WaMoS system is installed at the northwest corner on the platform in the background. In the radar images, several shadows are visible, which are due to the equipment of the platform. The large backscatter in the south originates from the oil field visible in the foreground of the photo. A wave rider buoy is placed near the oil field and within the radar measuring range. The two laser sensors are mounted on the main complex.

the investigations, only areas representing backscatter from the sea surface are considered. The range-ring patterns in the near range are caused by antenna-side lobe interactions with the ocean surface in the near field, and multiple reflections of the antenna side lobes in the near field from the host platform equipment in a distance of about 500 m, due to the longer running time of the radiated energy. To negate this effect, the data are corrected by the antenna pattern.

[13] The analogue output of the radar systems video signal is sampled by a Digital Scan Converter (DSC) with a sampling frequency of $f_{AD} = 20$ Mhz. The sampling frequency gives a radial resolution of $\Delta r = c/(2f_{AD}) = 7.5$ m, where c denotes the speed of light. In the near range of the antenna (0–240 m) the radar signal has not reached the water surface due to the limited vertical directivity and the installation height. There is no backscatter in this so-called dead range area. Therefore the DSC is delayed so as to detect only the radar backscatter from the end of the dead range. This area is visible in the radar image in Figure 1. With 256 samples in range, the covered area by the antenna is from 240 m to ≈ 2160 m.

[14] Nautical radar systems are equipped with a logarithmic amplifier and are not radiometrically calibrated. Therefore the normalized RCS could not be determined. The backscattered signal of each radar resolution cell is digitized with 8 bit, which allows gray values between 0 (no backscatter) and 255 (highest signal).

[15] Radar data sets with colocated in situ data were available for the investigations during 2001. The significant wave height during that period was up to $H_S \approx 7$ m. The wind speed was up to ≈ 17 m s⁻¹. Under these conditions,

there will be little or no white-capping of the waves, so that this effect, which causes an increase of the RCS, can be neglected.

[16] The in situ data, provided by one wave-rider buoy and two laser sensors (see Figure 1), are continuous measurements of the sea surface elevation, whereas the sea state parameters are determined for time intervals of 20 min. The sampling frequency is 2 Hz.

[17] Information about the precipitation has not been recorded. The reduction of the radar backscatter from the sea surface due to oil spills can be neglected.

3. Modulation Mechanisms

[18] The sea state is imaged by a radar, because the RCS of the ocean surface is modulated by the long surface gravity waves, which are within the resolution of the radar. This modulation of the RCS is mathematically described for local amplitudes by the modulation transfer function (MTF), which is defined as expansion of the RCS for the spectral amplitudes of the wave field $\hat{\eta}(\vec{k})$ [Alpers *et al.*, 1981],

$$\sigma_0 = \bar{\sigma}_0 + \delta\sigma_0 = \bar{\sigma}_0 \cdot \left(1 + \int M(\vec{k}) \cdot e^{j(\vec{k} \cdot \vec{r} - \omega(\vec{k}) \cdot t)} d\hat{\eta}(\vec{k}) \right), \quad (1)$$

with the mean RCS $\bar{\sigma}_0$, the modulation part $\delta\sigma_0$, the wave number vector \vec{k} and the angular frequency $\omega(\vec{k})$. The MTF is hermitian as well as the spectral amplitudes because of the real-valued RCS ($M(-\vec{k}) = M^*(\vec{k})$), and therefore also includes the phase information of the imaged ocean waves. The MTF is a sum of the contributing processes: the

geometrical effects of shadowing and tilt, hydrodynamic modulation, and wind modulation,

$$M = M_{wind} + M_{tilt} + M_{hydr} + M_{shad}. \quad (2)$$

[19] The wind modulation is based on the variation of the wind-induced friction velocity along the ocean surface, which is generating the small-scale roughness of the sea surface and raising the variance of the mean RCS $\bar{\sigma}_0$. Estimates of the modulation of the friction velocity have been carried out by *Hara and Plant* [1994]. They found that the influence of wind modulation on Bragg waves is stronger than on the longer ocean waves. By integrating a radar-image sequence over time, signatures with higher variability in time (like surface waves) are averaged out. Only static patterns such as the shadows from the towers and the wind signatures remain visible. The mean RCS of a radar-image sequence consists therefore mainly of the mean wind information. Further investigations on wind modulation have been performed by *Wright and Keller* [1980], *Smith* [1990], *Romeiser et al.* [1997], and *Romeiser and Alpers* [1997].

[20] Tilt modulation is a purely geometric effect which leads to a higher radar backscatter from a wave front which is directed toward the radar. The long ocean waves tilt the facets from the horizontal plane toward and away from the radar. This leads to a change of local incidence angles and therefore to a change of radar backscatter, which increases with decreasing incidence angle. The expansion of the RCS for the local tilt components is given by [*Alpers et al.*, 1981]

$$\begin{aligned} \left(\frac{\delta\sigma_0}{\bar{\sigma}_0} \right) &= \frac{1}{\bar{\sigma}_0} \cdot \left. \frac{\partial\sigma_0}{\partial\vec{n}} \right|_{\vec{n}=(0,0,1)} \cdot \vec{n} \\ &= \frac{1}{\bar{\sigma}_0} \cdot \left(\left. \frac{\partial\sigma_0(\Theta, \varphi, \delta=0)}{\partial \tan \varphi} \right|_{\varphi=0} \frac{\partial\eta}{\partial x} \right. \\ &\quad \left. + \left. \frac{\partial\sigma_0(\Theta, \varphi=0, \delta)}{\partial \tan \delta} \right|_{\delta=0} \frac{\partial\eta}{\partial y} \right), \end{aligned} \quad (3)$$

where \vec{n} is the vector perpendicular to the ocean surface, $\tan \varphi = \partial\eta/\partial x$ gives the tilt component of the surface in the plane of incidence, and $\tan \delta = \partial\eta/\partial y$ is the tilt component perpendicular to this plane. The relative angle between the wave propagation direction and the antenna viewing direction has a strong influence on the tilt modulation. Thereby the strongest modulation occurs for the tilt component of the ocean surface waves in antenna viewing direction or 180° to it. Therefore, if the wave crests are parallel to the antenna viewing direction, there is no modulation contribution [*Moore*, 1985].

[21] The hydrodynamic modulation describes the modulation of the amplitude and phase of the capillary waves by the interaction with the orbital velocity field of the long surface waves. This effect is indicated by convergence zones on the wave fronts and divergence zones on the wave back. The resulting modulation of spectral density of the Bragg waves is described by a two-scale model [*Alpers and Hasselmann*, 1978] and an improved three-scale model [*Romeiser et al.*, 1994]. Under grazing incidence at HH polarization, the discrete scattering elements are mainly contributing to the RCS of the ocean surface. These elements are increased by the hydrodynamic modulation [*Shyu and Phillips*, 1990].

[22] Shadowing is also a purely geometrical effect that appears under grazing incidence. Thereby parts of the imaged sea surface cannot be seen by the radar; they are shadowed by the waves. Shadowing appears, if the shadowing parameter, defined to be the ratio between the root mean square tilt of the sea surface and the depression angle $\Psi = 90^\circ - \Theta$, has values $\eta_s \geq 1$ [*Bass and Fuks*, 1979]. Thereby the wave amplitudes have to be high enough. In the case of Ekofisk, with an antenna height of 74 m, this modulation mechanism appears only in the very far range. Θ denotes the incidence angle, describing the angle between the perpendicular of the ocean surface and the radar beam.

[23] The developed empirical method for the determination of the ocean surface is based on the assumption that the RCS is mainly modulated by the wind and the ocean surface tilt,

$$M = M_{aero} + M_{tilt}. \quad (4)$$

The hydrodynamic modulation is neglected here, and shadowing is assumed to have a minor contribution to the RCS, because of the given antenna height.

[24] At X-band and HH polarization the mean RCS is (linear or nonlinear) dependent on the local depression angle [*Trizna and Carlson*, 1996]. This dependency is parameterized as a look-up table. The idea is that the deviation of the RCS from the mean RCS represents a local and temporal change of the depression angle, which is assumed to be equal to the local ocean surface tilt.

[25] For a local facet at location \vec{r} and time t the local RCS is given by

$$\begin{aligned} \sigma_0(\vec{r}, t) &= \bar{\sigma}_0(\vec{r}, t) + \delta\sigma_0(\vec{r}, t) \\ &= \bar{\sigma}_0(\vec{r}, t) \cdot \left(1 + M(\vec{k}|\vec{r}, t) \cdot \underbrace{e^{i\vec{k}\cdot\vec{r}} \cdot A(\vec{r}, t)}_{\eta(\vec{r}, t)} \right), \end{aligned} \quad (5)$$

describing the deviation of the RCS $\delta\sigma_0$ at location \vec{r} and time t as a product of the local modulation function $M(\vec{k}|\vec{r}, t)$ and the local wave field $\eta(\vec{r}, t)$ as indicated in equation (5). Thereby the local wave field is a product of a carrier wave with wave number \vec{k} and a slowly varying amplitude function $A(\vec{r}, t)$. This translation of the RCS to the local surface tilt is a local, spatial, and temporal description of the modulation process. The MTF is therefore a spatial and temporal function, which has to be determined for each location. This is different from the description of the MTF in the spectral domain regarding equation (1).

4. Method

[26] This chapter describes the steps of the empirical method for retrieving the ocean surface from radar-image sequences. The input for the method are the raw polar radar-image sequences $G(\vec{r}, t)$ acquired by the WaMoS system. The method is demonstrated with the radar-image sequence in Figure 2, recorded on June 3, 2001, at Ekofisk 2/4k.

4.1. Radar Pattern

[27] Nautical radar antennas are directional antennas, which radiate radio-frequency energy in patterns of lobes

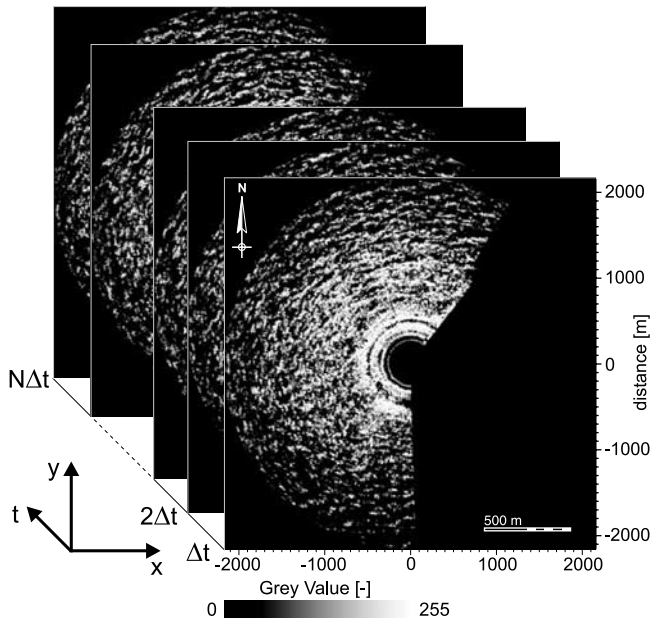


Figure 2. Radar-image sequence recorded on June 3, 2001, at Ekofisk 2/4k.

or beams that extend outward from the radar antenna in one direction for a given antenna position. The radiation pattern also contains minor lobes, but these are weak and normally have little effect on the main radiation pattern. However, in the case of Ekofisk, range-ring patterns appear in the near range (Figure 1), caused by multiple reflections of these antenna side lobes in the near field from the host platform equipment as mentioned already in section 2. The main lobe

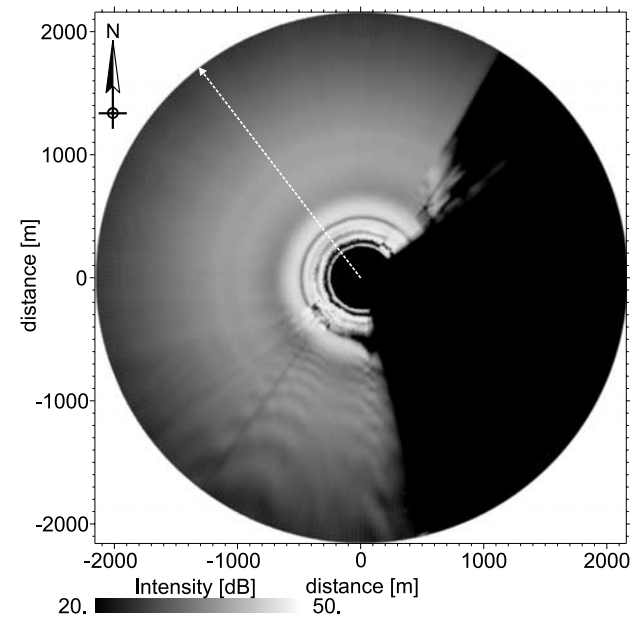


Figure 3. Determined antenna receiving pattern of the radar system mounted on the Ekofisk 2/4k platform. The image still contains an additional RCS term due to wind modulation. The dashed line indicates the cut shown in Figure 4.

varies in angular width 0.9° and vertically 21° . Because of the radiation pattern, each radar antenna has a typical receiving pattern. An important step to analyze the radar data is to know this receiving pattern and to correct the data.

[28] For measuring, the antenna receiving pattern radar images have to be measured in an area that provides a homogeneous RCS over the entire measurement area. For synthetic aperture radar images this is done by taking images from the rain forests. For the nautical radar system it is not possible to take measurements like this. By taking the total time average of the radar images of all given data sets from the Ekofisk installation, the radar-typical receiving pattern is determined with an additional constant RCS term due to wind modulation as shown in Figure 3. By transforming the total mean RCS image into the spectral domain with a 2-D Fast Fourier Transform (FFT), the constant term is filtered out. After applying an inverse 2-D FFT, the antenna pattern is determined. Figure 4 shows the result, a 1-D radial cut through the 2-D antenna receiving pattern (Figure 3), beginning at the image center.

[29] All images of a given radar-image sequence $G(\vec{r}, t)$ are corrected with the 2-D antenna pattern. Figure 5 is exemplary, showing a corrected radar image of the sequence of 32 images.

4.2. Parameterization of Mean RCS

[30] The mean radar cross section (RCS) is dependent on the local depression angle at X-band and HH polarization [Trizna and Carlson, 1996]. Regarding equation (3), the deviation of the RCS $\delta\sigma_0$ from the mean RCS $\bar{\sigma}_0$ represents a local and temporal change of the depression angle, which is assumed to be equal to the local ocean surface tilt.

[31] Therefore the dependency between the mean RCS and the depression angle has to be parameterized to derive the ocean surface tilt. Because the radar is imaging the ocean surface beam by beam, and the radar is mainly imaging waves traveling toward or away from the radar, an effective way for the parameterization of the mean RCS is 1-D for each radar beam. This is performed by fitting a

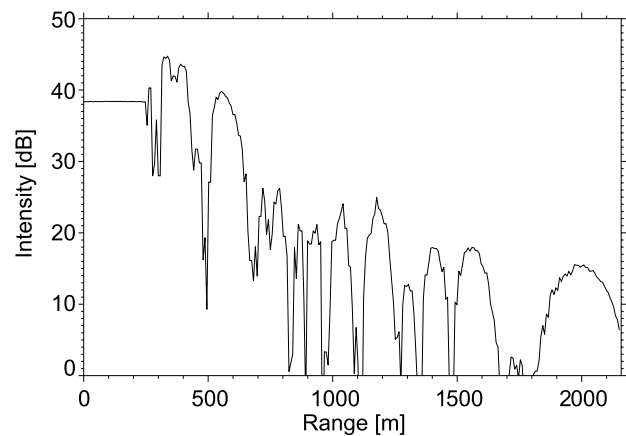


Figure 4. A 1-D radial cut through the 2-D antenna receiving pattern of Figure 3, beginning at the center of the image. The constant RCS term due to wind modulation has been removed. The dead range is from 0–240 m and is not considered here.

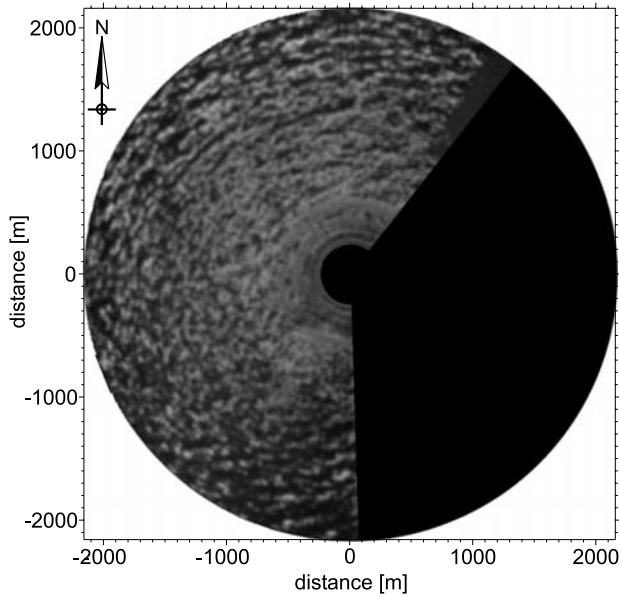


Figure 5. Sample image of the radar-image sequence, recorded on June 3, 2001, at Ekofisk 2/4k, corrected by the radar receiving pattern.

third-order polynomial curve $f(r, \phi_i)$ through the mean RCS $\bar{\sigma}_0$ for each look direction ϕ_i ,

$$\tilde{\sigma}_{0,i}(r, \phi_i) = f(r, \phi_i). \quad (6)$$

Here $\tilde{\sigma}_0$ gives the resulting 2-D fitting polynomial, built up beam by beam in azimuth (i denotes the beam number), by using a least squares method. Figure 6 shows exemplarily the approximation of the mean RCS.

[32] Additionally to the parameterization of the mean RCS, the local radar depression angle is required. For a given installation height of the radar antenna $h_{ant} = 74$ m, the range-dependent depression angle $\tilde{\Psi}$ is given by

$$\tilde{\Psi}(r) = \arctan\left(\frac{h_{ant}}{r}\right), \quad (7)$$

with r giving the distance from the antenna. The depression function is shown in Figure 7. Both parameterizations

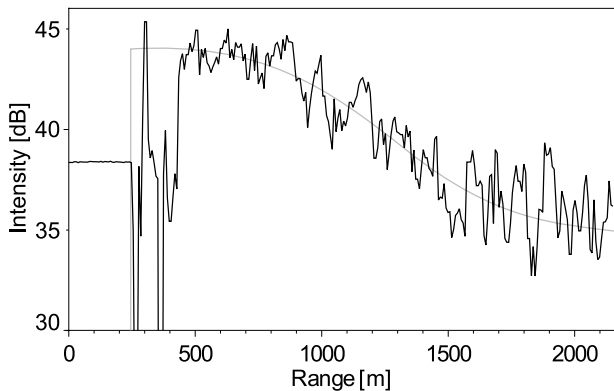


Figure 6. Parameterization $\tilde{\sigma}_{0,i}(r, \phi_i)$ (gray) of the mean RCS $\bar{\sigma}_0(r, \phi_i)$ of one radar beam for the first image of the radar-image sequence, corrected by the radar receiving pattern.

together give the relationship between the RCS and the depression angle in range and azimuth direction.

4.3. Determination of Tilt Angle

[33] The local deviation of the RCS $\delta\sigma_0$ from the mean RCS is caused by tilt modulation of the RCS due to the ocean surface waves. This local deviation causes a local change of the depression angle $\delta\Psi$, which is assumed to be equal to the local ocean surface tilt φ .

[34] At a given distance from the antenna, for a certain radar beam (r_0, ϕ_i) , the tilt angle φ is retrieved by determining the difference of the depression angles,

$$\varphi(r_0, \Psi_i) = \delta\Psi = \Psi_1(r_0, \phi_i) - \Psi_0(r_0, \phi_i), \quad (8)$$

where Ψ_1 is the depression angle at that distance from the antenna r , where the parameterization $\tilde{\sigma}_0$ regarding equation (6) is equal to the given RCS $\sigma_0(r_0) = \bar{\sigma}_0(r_0) + \delta\sigma_0(r_0)$,

$$\Psi_1(r_0, \phi_i) = \tilde{\Psi}\left(f_{\tilde{\sigma}_{0,i}}^{-1}(\sigma_0, \phi_i)\right). \quad (9)$$

Ψ_0 is the depression angle at r_0 ,

$$\Psi_0(r_0, \phi_i) = \tilde{\Psi}(r_0). \quad (10)$$

In Figure 8 the resulting tilt angles for one radar beam are exemplarily shown. The tilt angles vary within the given range of the depression angles. For RCS values σ_0 exceeding the domain of $\tilde{\sigma}_0$, the limit values of $\tilde{\Psi}$ are assigned. The mean tilt angle has to be zero. Deviations from this value, as can be seen in this example, are caused by the limitations of the chosen simple polynomial parameterization.

[35] The local tilt angles are determined for each radar image of a radar-image sequence. The result is a sequence of tilt images $\Phi(\vec{r}, t)$.

4.4. Determination of Ocean Surface Elevation

[36] The ocean surface elevation $\eta(\vec{r}, t)$ is determined from the tilt angles $\Phi(\vec{r}, t)$ directly by integration over the space coordinates \vec{r} . In the spatial domain the integration is performed by convolving the tilt images with a 2-D integration filter kernel. A convolution in the spatial domain corresponds to a multiplication in the Fourier space. This is

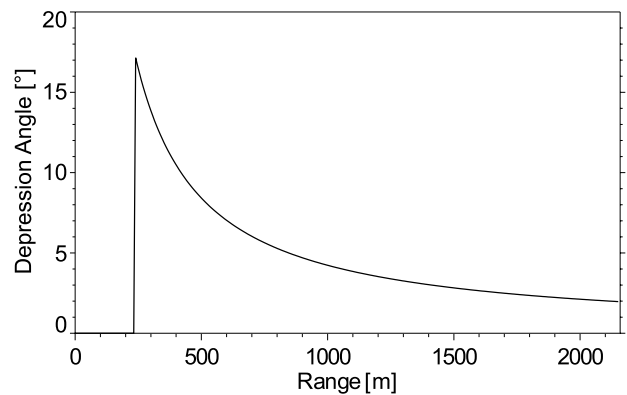


Figure 7. Range-dependent depression angle for a given antenna height of 74 m above the mean sea level at Ekofisk 2/4k.

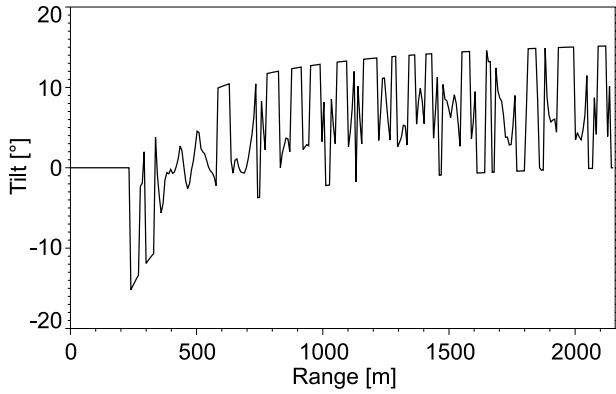


Figure 8. Range-dependent tilt angle for a given antenna height of 74 m above the mean sea level at Ekofisk 2/4k.

an effective method for the numerical integration. The transfer function of an ideal integration filter is purely imaginary and proportional to the wave number,

$$\hat{D} = ik^{-1} |\cos(\phi_W - \phi_A)|^{-1} \quad k > 0, \quad (11)$$

where k gives the modulus of the wave number vector \vec{k} , Φ_W is the wave travel direction and ϕ_A the antenna look direction. The function is complex and shifts the phase of all wave number components in the Fourier space by $\pi/2$. The smaller the wave numbers are, the more they are amplified. The modulus of the wave numbers depends on the wave travel direction relative to the antenna look direction.

[37] The tilt-image sequence $\Phi(\vec{r}, t)$ is transformed in the wave number frequency domain with a 3-D FFT. The resulting complex 3-D spectrum $\hat{\Phi}(\vec{k}, \omega)$ of the tilt-image sequence is integrated by multiplying with the integration transfer function \hat{D} ,

$$\hat{\eta}(\vec{k}, \omega) = \hat{\Phi}(\vec{k}, \omega) \cdot \hat{D}. \quad (12)$$

The result is a complex 3-D wave spectrum of the ocean surface elevation field.

[38] As mentioned previously, the division by the wave numbers causes an asymptotically increase of the amplitudes for very small wave numbers. A filtering process is therefore necessary to retrieve only the signal of the ocean surface wave field itself when transforming the complex 3-D wave spectrum into the spatial-temporal domain. Otherwise the wave signal is overlaid by an interfering signal with high-amplitude and long wavelength.

[39] The signal of linear surface-gravity waves is well located on a surface in the wave number frequency domain defined by the dispersion relation of linear surface-gravity waves [Young *et al.*, 1985; Seemann, 1997],

$$\varpi = \sqrt{gk \tanh kd} + \vec{k} \cdot \vec{u}, \quad (13)$$

where ϖ indicates the absolute frequency, G is the gravitational acceleration, d is the water depth, and \vec{u} is the velocity of encounter, which is a sum of the platform velocity and the near-surface current velocity. The so-called dispersion shell connects the wave numbers k with their corresponding frequency coordinate ω . This function is used for a pre-selection of the Fourier coefficients in the complex

3-D wave spectrum of a multimodal wave field with image features that are not resulting from ocean surface waves,

$$\hat{\eta}_W(\vec{k}, \omega) = \delta(\omega - \varpi(\vec{k}; \vec{u}, d)) \hat{\eta}(\vec{k}, \omega). \quad (14)$$

As indicated by the δ -function, the water depth d and the velocity of encounter \vec{u} have to be determined for using the dispersion relation as filter. This is done by fitting the theoretical dispersion relation to the signal coordinates in the complex wave number frequency spectrum [Senet *et al.*, 2001; Outzen, 1998].

[40] To suppress those Fourier coefficients with small wave numbers and those with noise from non-relevant spectral components additionally a band-pass filter is applied. This is performed by a normalized 3-D Gabor filter, which has the advantage of reducing the filtering effects in temporal and spatial domain. A certain wave number and frequency range around the peak wave number k_0 and peak frequency ω_0 is selected using a Gaussian function,

$$\hat{\Omega}(k_x, k_y, \omega) = e^{-\pi(|k_x - k_{x0}|^2 \sigma_{k_x} + |k_y - k_{y0}|^2 \sigma_{k_y} + |\omega - \omega_0|^2 \sigma_\omega)}, \quad (15)$$

where σ_{k_x} , σ_{k_y} , and σ_ω are the standard deviations that define the filter bandwidth in the corresponding dimensions. The filter is similar to a windowed Fourier transformation with the Gaussian function as window function. In case there are several overlapping wave systems, a segmentation has to be performed. This can be done by applying the 3-D Gabor filter to every significant peak in the complex spectrum of the dominating wave systems.

[41] The 3-D Gabor filter is multiplied with the complex Fourier coefficients of the complex wave number frequency spectrum,

$$\hat{\eta}'_W(\vec{k}, \omega) = \hat{\Omega}(k_x, k_y, \omega) \cdot \hat{\eta}_W(\vec{k}, \omega). \quad (16)$$

The remaining complex Fourier coefficients are related to the linear surface gravity waves as indicated in Figure 9.

[42] To retrieve the wave field $\eta(\vec{r}, t)$, the complex 3-D wave spectrum $\hat{\eta}'_W(\vec{k}, \omega)$ is transformed in to the spatial-temporal domain by an inverse 3-D FFT. Figure 10 shows one resulting ocean surface elevation image of the sequence of 32 images, recorded on June 3, 2001, at Ekofisk 2/4k.

[43] An azimuthal dependency of the ocean surface elevation is clearly visible. This dependency is explained as a geometrical projection factor as follows: Only the tilt component of the water surface in the antenna viewing direction affects the modulation of the RCS. Therefore the RCS is not modulated if the radar is looking parallel to the wave crests. Determining the significant wave height for the area around the given wave travel direction from this image gives $H_S = 4.46$ m, which is in good agreement with $H_S = 4.86$ m, retrieved from a colocated time series, recorded by the wave rider buoy.

5. Validation

[44] This section focuses on the statistical and deterministic comparison of the ocean surface image sequences, retrieved by the method introduced in this paper, with the colocated measurements of three in situ sensors, one wave

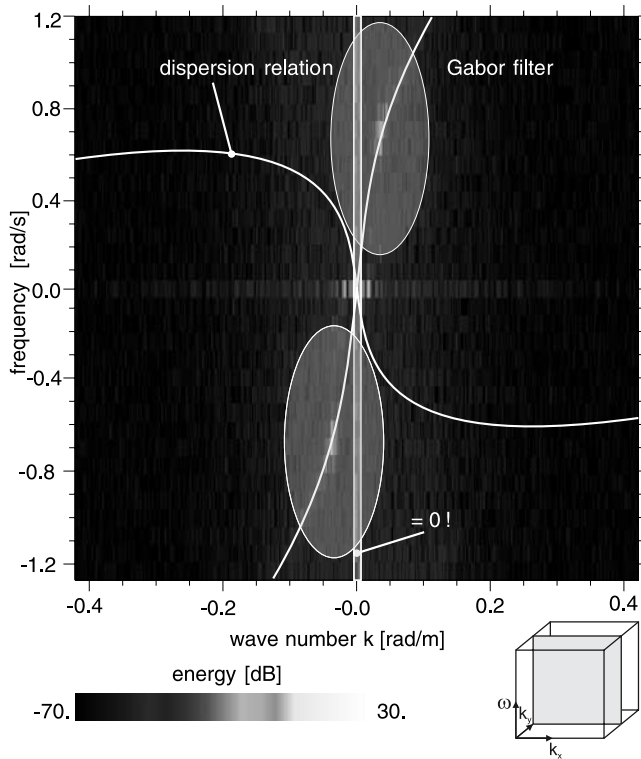


Figure 9. Cut through the wave number frequency spectrum (squared modulus). The signal of the linear ocean surface waves, located on the dispersion relation, is visible. Additionally, the Gabor filter is shown, to suppress the small wave numbers (vertical lines) and spectral noise components.

rider buoy and two laser sensors, which are installed within the measurement area of the radar. The direct deterministic comparison of an ocean surface elevation time series from the radar images and from the buoy gives an impression of the capabilities of this method. Furthermore, a spectral comparison is performed.

5.1. Statistical Comparison to In Situ Data

[45] The significant wave height H_S is the most important quantity used describing a sea state. H_S is used for evaluating the impact of waves and breakers onto watercraft, breakwaters, or harbor constructions, in the open sea and coastal zones. It is usually determined directly from a wave record in a number of ways. For the given ocean wave field image sequence $\eta(\vec{r}, t)$, retrieved from radar-image sequences, H_S is directly determined from the standard deviation of the spatial-temporal wave elevation,

$$H_{S,radar} = 4 \cdot \left\langle (\eta(r, \phi, t) - \bar{\eta})^2 \right\rangle^{\frac{1}{2}} \forall |\phi - (\phi_W \pm 180^\circ)| \leq 22.5^\circ, \quad (17)$$

where $\bar{\eta}$ gives the population mean, and $\langle \cdot \rangle$ denotes the expectation value of η . Because the radar is mainly imaging waves which travel toward and away from the radar, the significant wave height is determined only for the area within $\pm 22.5^\circ$ of the wave travel direction $\phi_W \pm 180^\circ$.

[46] For comparison, colocated 2-Hz time series of 20 min each from the three in situ sensors, one wave rider buoy and two laser sensors (“Flare North” and “Flare South”), are used. The location of all sensors is indicated in Figure 10. Two sensors, the buoy and laser “Flare North”, are within the radar measuring range. The buoy is located within the sea surface area visible by the radar. For the time series, the significant wave height is

$$H_{S,insitu} = 4 \cdot \left\langle (\eta(t) - \bar{\eta})^2 \right\rangle^{\frac{1}{2}}. \quad (18)$$

[47] In total, 77 radar data sets with significant wave heights up to 6 m are processed, together with their colocated time series from the in situ sensors. Figure 11 gives an intercomparison of the H_S values of the four sensors. The upper row shows the comparison of H_S from the three in situ sensors and from the radar. As expected, the best correlation and lowest standard deviation is found between wave rider buoy and laser “Flare North,” because they are located within the measuring area of the radar. The lower row of Figure 11 gives an intercomparison between all three in situ sensors. It can be seen that the correlation, bias, and standard deviation between the in situ sensors is within the same range as between the in situ sensors and the radar. Statistically, the accuracy of the determined H_S from the radar-retrieved ocean surface elevation image sequences is within the accuracy of the in situ sensors. The radar underestimates the in situ values only for small significant wave heights.

5.2. Deterministic Comparison to In Situ Data

[48] Because the wave rider buoy is situated within the line of view of the radar, a direct comparison of the time

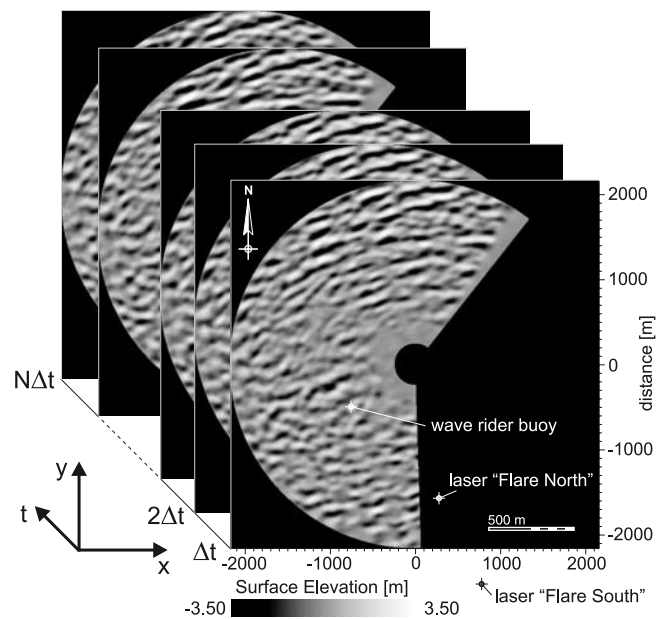


Figure 10. Ocean surface elevation sequence of the radar-image sequence recorded on June 3, 2001, at Ekofisk 2/4k (see Figure 2). The determined H_S from this image is 4.46 m compared to $H_S = 4.86$ m retrieved from a colocated time series from the wave rider buoy.

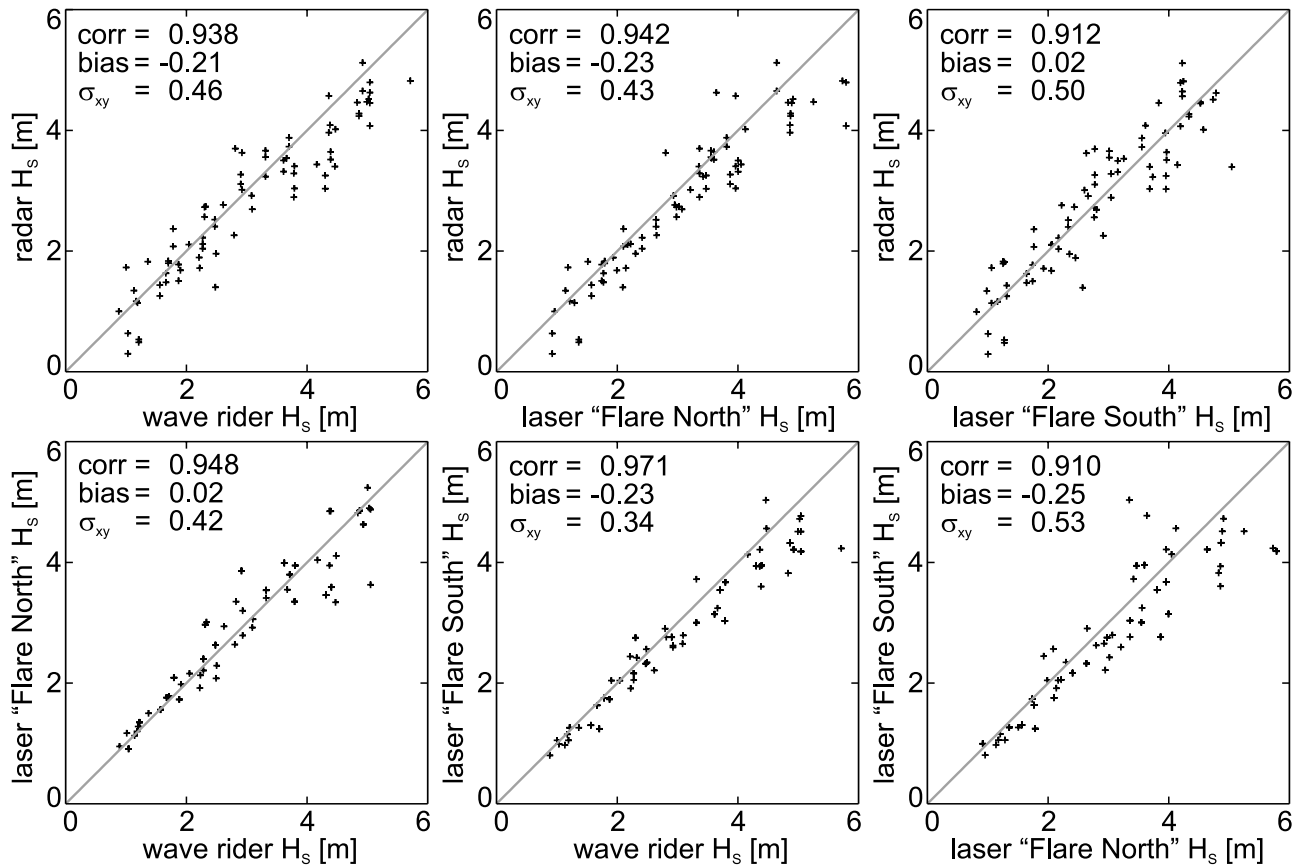


Figure 11. Intercomparison of significant wave heights derived from the inverted radar-image sequences and colocated wave records from three in situ sensors, a wave rider buoy and the lasers “Flare North” and “Flare South,” located in the Ekofisk oil field.

series of wave elevation, recorded by the buoy $\eta_{buoy}(t)$ and retrieved from the radar-image sequences $\eta_{radar}(\vec{r}_{buoy}, t)$, is possible. The location of the buoy is indicated by \vec{r}_{buoy} and shown in Figure 10. For comparison, the radar-image sequence as seen in Figure 2, recorded on June 3, 2001, 1015:00 UTC at Ekofisk 2/4k, has been transformed to the ocean surface elevation image sequence by the introduced inversion method. For this date and the given starting time

of the radar record, the colocated buoy time series is taken. With a sampling period of $\Delta t_{radar} = 2.56$ s and 32 images (samples) per radar data set, the total time duration is $T_{tot} \approx 82$ s. The buoy record has a sampling period of $\Delta t_{buoy} = 0.5$ s (2 Hz). Therefore 164 samples are taken for the given total time duration T_{tot} of the radar data set. The internal clocks of both, radar and buoy system, are not synchronized, but are setup with UTC time. A temporal synchronization

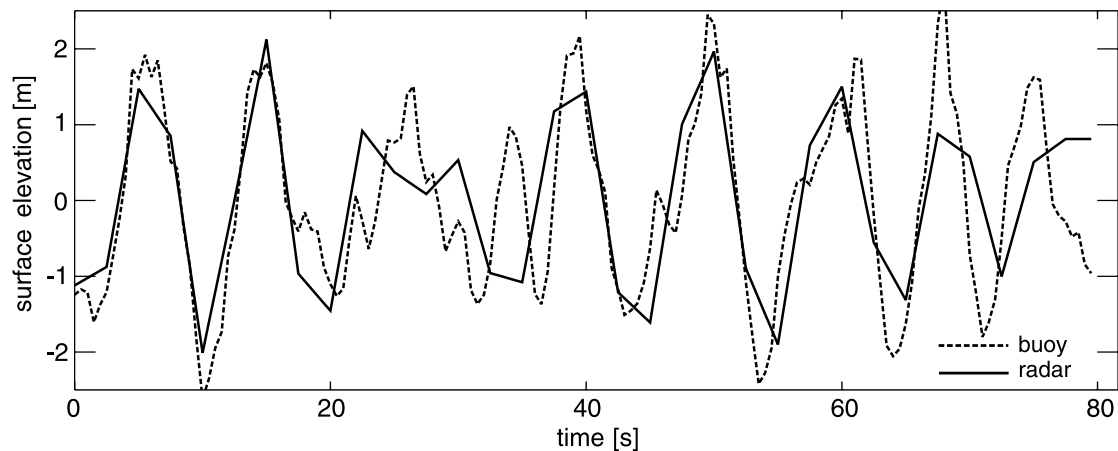


Figure 12. Synchronized wave elevation time series derived from radar wave elevation time series (solid curve), and a colocated buoy record (dashed curve). The data sets were recorded on June 3, 2001, $1015:00 \pm 1$ s at Ekofisk 2/4k.

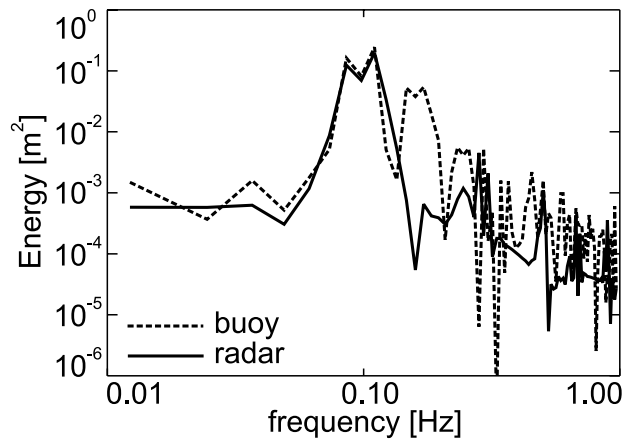


Figure 13. Frequency power spectra of the time series of Figure 12.

procedure between both data sets is therefore necessary. For the analyzed case, the recorded start time differed by 2 s. Figure 12 shows the overlaid and synchronized time series. The solid curve is the radar-retrieved record at the buoy's location, and the dashed curve is the colocated buoy record. Overall, the time series show a good agreement. The amplitudes are within the same range, and the periods are the same. There is no phase decorrelation.

[49] This transect in space and time allows the investigation of single wave properties, such as wave height, steepness, etc. Following the zero-up crossing definition for time series, the second wave in the records in Figure 12 is identified as the highest wave with $H \approx 4$ m, beginning at about 10 s. With a wave period of $T \approx 10$ s, the wave steepness ϵ is

$$\epsilon = H/L \approx 0.64 \cdot H/T^2 = 0.026. \quad (19)$$

Figure 13 illustrates the comparison of the frequency energy spectra derived from the radar wave elevation map (solid curve), and the buoy record (dashed curve). Both spectra present a good agreement, whereas the radar spectrum is more narrow-banded, due to the band-pass filtering during

processing. The peak frequency is in both records at $f_p \approx 0.1$ Hz (10 s), with the same value for the energy maximum.

[50] Figure 14 exemplarily shows a spatial cut through the last of the 32 ocean surface elevation images of the analyzed radar data set. There is a dominant wave group visible traveling southward. The highest wave, which is found within the group, has a wave height of $H \approx 5$ m. The wavelength is $L \approx 180$ m, and the steepness $\epsilon = H/L = 0.028$. Wave groups play an important role for the design and assessment of offshore platforms, breakwaters, or ships, because successive large single wave crests or deep troughs can cause severe damages due to their impact, or they can excite the resonant frequencies of the structures. For ships, an encounter with wave groups can sometimes cause capsizing or severe damage. Therefore the detection of wave groups in space and time is of extreme importance for ocean engineers and scientists. For a detailed work on retrieval and investigations of the properties of individual spatial-temporal wave groups from ocean surface elevation image sequences, the reader is referred to *Dankert et al.* [2003a].

6. Conclusions

[51] The empirical inversion method introduced here allows the derivation of sequences of ocean surface elevation maps from radar-image sequences. The inversion scheme is based on the determination of the tilt angle of the ocean surface at each pixel of the radar images. The mean RCS depends on the mean local depression angle. The deviation of the RCS from the mean RCS represents a local and temporal change of the depression angle, which is assumed to be equal to the local ocean surface tilt. The modulation of the RCS by the ocean surface tilt is described locally, spatially, and temporally. Hydrodynamic modulation and the geometrical effect of shadowing are neglected here.

[52] The radar images are acquired using a conventional nautical X-band radar with HH polarization at grazing incidence. The method represents an extension of the existing techniques for deriving wave spectra and sea state parameters and is seen as an alternative to the inversion

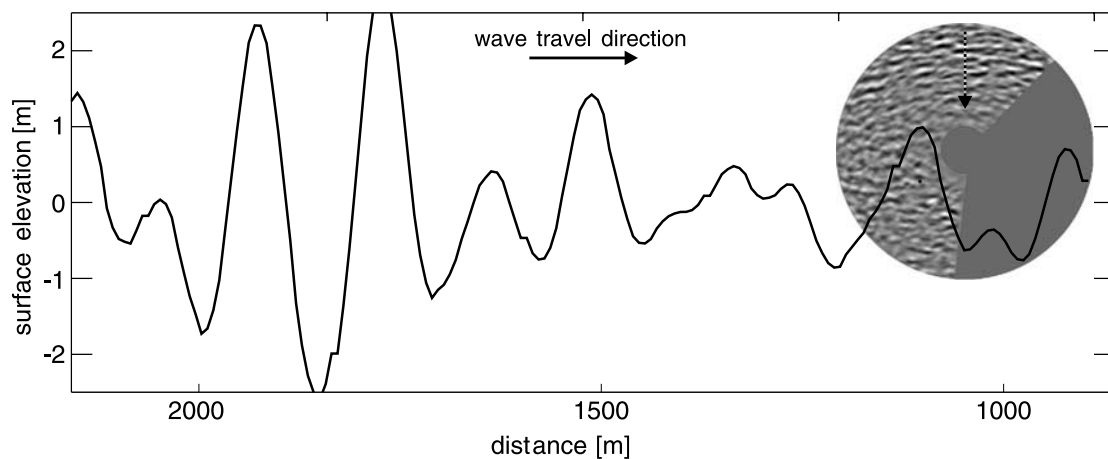


Figure 14. Spatial cut through the last of the 32 ocean surface elevation images derived from radar-image sequence, recorded on June 3, 2001, at Ekofisk 2/4k. The position and direction of the cut is indicated in the elevation map.

scheme as proposed by Borge *et al.* [2004]. Different from Borge *et al.* [2004], the radar system does not need in situ sensors. A calibration procedure is not necessary.

[53] The inversion scheme was applied to radar data sets, recorded by the WaMoS system from a platform in the Ekofisk oil field in the central North Sea. For validation of the method, colocated measurements from three in situ sensors, one wave rider buoy and two laser sensors, were taken. In a first validation phase a statistical wave parameter, the significant wave height, has been determined from the radar-derived time series of ocean surface elevation maps and compared to the significant wave height from colocated in situ wave records. Furthermore, an intercomparison between all four sensors has been performed. Thereby correlation, bias, and standard deviation between the in situ sensors is within the same range as between the in situ sensors and the radar. Therefore it could be shown that the accuracy of the radar-retrieved ocean surface elevation image sequences is within the accuracy of the in situ sensors. The radar underestimates the in situ values only for small significant wave heights.

[54] A wave profile measured by the buoy was compared to the colocated radar-derived ocean surface at the location of the buoy. The shown transects in space and time demonstrated the capabilities of the inversion method for studying single wave properties, such as wave height or wave steepness, spatially and temporally. Furthermore, wave groups are detectable and investigatable in space and time from the radar-derived time series of ocean surface elevation maps, which has previously been done by Dankert *et al.* [2003a]. Recently, further investigations on the azimuthal dependency of the RCS were performed regarding the imaging of azimuthal traveling waves with the aim of retrieving the correct ocean surface elevation for the whole measurement area.

[55] **Acknowledgments.** This work was carried out in the framework of the European project MAXWAVE (project evk: 3-2000-00544). The radar-image sequences were kindly made available by the company OceanWaves.

References

- Alpers, W., and K. Hasselmann (1978), The two-frequency microwave technique for measuring ocean wave spectra from an airplane or satellite, *Boundary Layer Meteorol.*, *13*, 215–230.
- Alpers, W., and K. Hasselmann (1982), Spectral signal to clutter and thermal noise properties of ocean wave imaging synthetic aperture radars, *Int. J. Remote Sens.*, *3*, 423–446.
- Alpers, W. R., D. B. Ross, and C. L. Rufenach (1981), On the detectability of ocean surface waves by real and synthetic aperture radar, *J. Geophys. Res.*, *86*, 6481–6498.
- Bass, F., and I. Fuks (1979), *Wave Scattering from Statistically Rough Surfaces*, Pergamon, New York.
- Bell, P. (1999), Shallow water bathymetry derived from an analysis of x-band marine radar images of waves, *Coastal Eng.*, *37*, 513–527.
- Borge, J. N., K. Hessner, and K. Reichert (1999), Estimation of the significant wave height with x-band nautical radars, *Proceedings of the 18th International Conference on Offshore Mechanics and Arctic Engineering (OMAE)*, OMAE99/OSU-3063, St. John's, Newfoundland, Canada.
- Borge, J. N., G. Rodríguez, K. Hessner, and P. González (2004), Inversion of marine radar images for surface wave analysis, *J. Atmos. Oceanic Technol.*, in press.
- Dankert, H. (2003), Retrieval of surface-current fields and bathymetries using radar-image sequences, paper presented at International Geoscience Remote Sensing Symposium, Inst. of Elect. and Elect. Eng., Hamburg, Germany.
- Dankert, H., J. Horstmann, S. Lehner, and W. Rosenthal (2003a), Detection of wave groups in SAR images and radar-image sequences, *IEEE Trans. Geosci. Remote Sens.*, *41*(6), 1437–1446.
- Dankert, H., J. Horstmann, and W. Rosenthal (2003b), Ocean wind fields retrieved from radar-image sequences, *J. Geophys. Res.*, *108*(C11), 3352, doi:10.1029/2003JC002056.
- Hara, T., and W. J. Plant (1994), Hydrodynamic modulation of short wind-wave spectra by long waves and its measurement using microwave backscatter, *J. Geophys. Res.*, *99*, 9767–9784.
- Lee, P., et al. (1995), X-band microwave backscattering from ocean waves, *J. Geophys. Res.*, *100*, 2591–2611.
- Moore, R. (1985), Radar sensing of the ocean, *IEEE J. Oceanic Eng.*, *10*, 84–112.
- Outzen, O. (1998), Bestimmung der Wassertiefe und der oberflächennahen Strömung mit einem nautischen Radar (in German), Diploma thesis, Univ. of Hamburg, Germany.
- Plant, W. (1991), The variance of the normalized radar cross section of the sea, *J. Geophys. Res.*, *96*, 20,643–20,654.
- Romeiser, R., and W. Alpers (1997), An improved composite surface model for the radar backscattering cross section of the ocean surface: 2. Model response to surface roughness variations and the radar imaging of underwater bottom topography, *J. Geophys. Res.*, *102*, 25,251–25,267.
- Romeiser, R., A. Schmidt, and W. Alpers (1994), A three-scale composite surface model for the ocean wave—radar modulation transfer function, *J. Geophys. Res.*, *99*, 9785–9801.
- Romeiser, R., W. Alpers, and V. Wisman (1997), An improved composite surface model for the radar backscattering cross section of the ocean surface: 1. Theory of the model and optimization/validation by scatterometer data, *J. Geophys. Res.*, *102*, 25,237–25,250.
- Seemann, J. (1997), Interpretation der Struktur des Wellenzahl-Frequenzspektrums von Radar-Bildsequenzen des Seegangs (in German), dissertation, Univ. of Hamburg, Germany.
- Senet, C., J. Seemann, and F. Ziemer (2001), The near-surface current velocity determined from image sequences of the sea surface, *IEEE Trans. Geosci. Remote Sens.*, *39*, 492–505.
- Shyu, J.-H., and O. Phillips (1990), The blockage of gravity and capillary waves by longer waves and currents, *J. Fluid. Mech.*, *217*, 115–141.
- Smith, J. (1990), Modulation of short wind waves, in *Surface Waves and Fluxes*, pp. 247–284, Kluwer Acad., Norwell, Mass.
- Trizna, D. (1997), A model for brewster angle effects on sea surface illumination for sea scatter studies, *IEEE Trans. Geosci. Remote Sens.*, *35*, 1232–1244.
- Trizna, D. (2001), Errors in bathymetric retrievals using linear dispersion in 3-D fit analysis of marine radar ocean wave imagery, *IEEE Trans. Geosci. Remote Sens.*, *39*, 2465–2469.
- Trizna, D., and D. Carlson (1996), Studies of dual polarized low grazing angle radar sea scatter in nearshore regions, *IEEE Trans. Geosci. Remote Sens.*, *34*, 747–757.
- Wetzel, L. (1990), Electromagnetic scattering from the sea at low grazing angles, in *Surface Waves and Fluxes*, vol II, edited by G. L. Geernaert and W. J. Plant, pp. 109–171, Kluwer Acad., Norwell, Mass.
- Wright, J., and W. Keller (1980), Ocean-wave modulation transfer functions from the West Coast experiment, *J. Geophys. Res.*, *85*, 4957–4966.
- Young, I., W. Rosenthal, and F. Ziemer (1985), A three-dimensional analysis of marine radar images for the determination of ocean wave directionality and surface currents, *J. Geophys. Res.*, *90*, 1049–1059.
- Ziemer, F. (1995), An instrument for the survey of the directionality of the ocean wave field, in *Proceedings of the WMO/IOC Workshop on Operational Ocean Monitoring Using Surface-Based Radars*, vol. 32, pp. 81–87, World Meteorol. Org., Geneva, Switzerland.

H. Dankert and W. Rosenthal, Institute for Coastal Research, GKSS Research Center, Max-Planck-Strasse 1, Building 11, 21502 Geesthacht, Germany. (dankert@gkss.de)